Article

Parallel Proteomic and Transcriptomic Microenvironment Mapping (μMap) of Nuclear Condensates in Living Cells

Steve D. Knutson, Chenmengxiao Roderick Pan, Niels Bisballe, Brandon J. Bloomer, Philip Raftopolous, Iakovos Saridakis, and David W. C. MacMillan*

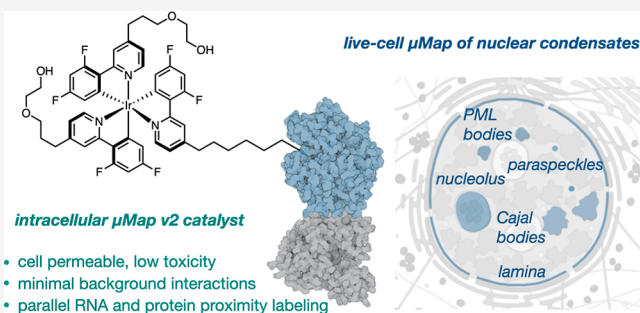Read Online

ACCESS | Metrics & More | Article Recommendations | SI Supporting Information

ABSTRACT: Cellular activity is spatially organized across different organelles. While several structures are well-characterized, many organelles have unknown roles. Profiling biomolecular composition is key to understanding function but is difficult to achieve in the context of small, dynamic structures. Photoproximity labeling has emerged as a powerful tool for mapping these interaction networks, yet maximizing catalyst localization and reducing toxicity remains challenging in live cell applications. Here, we disclose a new intracellular photocatalyst with minimal cytotoxicity and off-target binding, and we utilize this catalyst for HaloTag-based microenvironment-mapping (μMap) to spatially catalog subnuclear condensates in living cells. We also specifically develop a novel RNA-focused workflow (μMap-seq) to enable parallel transcriptomic and proteomic profiling of these structures. After validating the accuracy of our approach, we generate a spatial map across the nucleolus, nuclear lamina, Cajal bodies, paraspeckles, and PML bodies. These results provide potential new insights into RNA metabolism and gene regulation while significantly expanding the μMap platform for improved live-cell proximity labeling in biological systems.

live-cell μMap of nuclear condensates

intracellular μMap v2 catalyst
- cell permeable, low toxicity
- minimal background interactions
- parallel RNA and protein proximity labeling

PML bodies, paraspeckles, nucleolus, Cajal bodies, lamina

INTRODUCTION

Membraneless organelles and condensates have challenged traditional perspectives on cellular physiology and emerged as key players in regulating gene expression and cell function.[1,2] Dysregulation of condensate formation and function is also strongly linked with neurodegenerative disease pathologies and several cancer types.[3,4] However, many basic physical principles of phase-separated organelles and their phenotypic roles are not well understood. Characterizing these structures would both elucidate basic cellular mechanisms and enable the design of novel therapeutics for several disease classes. Despite this importance, the central difficulty lies in studying these highly dynamic and compositionally complex structures.

Our laboratory recently introduced microenvironment mapping (μMap)[5] as a high-resolution proximity labeling technology whereby blue light-induced energy transfer from iridium (Ir) photocatalysts to biotin-diazirine probes generates broadly reactive carbenes to label nearby biomolecules at nanometer resolution (Figure 1a).[6] The μMap platform has effectively profiled cell-surface microenvironments,[5,7] small molecule drug targets,[8,9] chromatin interactomes in isolated nuclei,[10] and stress granule disassembly mechanisms.[11] However, we and other groups have observed significant mitochondrial accumulation of photocatalysts and toxicity in live-cell experiments, particularly with cationic Ir polypyridyl complexes.[12−14] Although advantageous for mitochondrial

profiling and photodynamic therapy,[15,16] this property reduces mapping efficiency in other locations and is a major hindrance in utilizing this platform in living cells or whole organisms across long time-scales. Addressing this limitation would represent a significant technological advance and enable profiling of virtually any subcellular structure in a variety of biological contexts.

RESULTS AND DISCUSSION

As an expanded general platform, we envisioned a chemogenetic labeling workflow wherein a protein-of-interest (POI) residing in a specific subcellular structure would be fused to HaloTag,[17] enabling photocatalyst attachment to tag proximal biomolecules. The high-resolution and broad reactivity of μMap could then be harnessed for simultaneous labeling of protein and RNA interactomes within condensates (Figure 1a,b), offering significant functional and mechanistic insights surrounding these structures. To design an improved platform, we first tested alternative catalysts. Hypothesizing that cationic
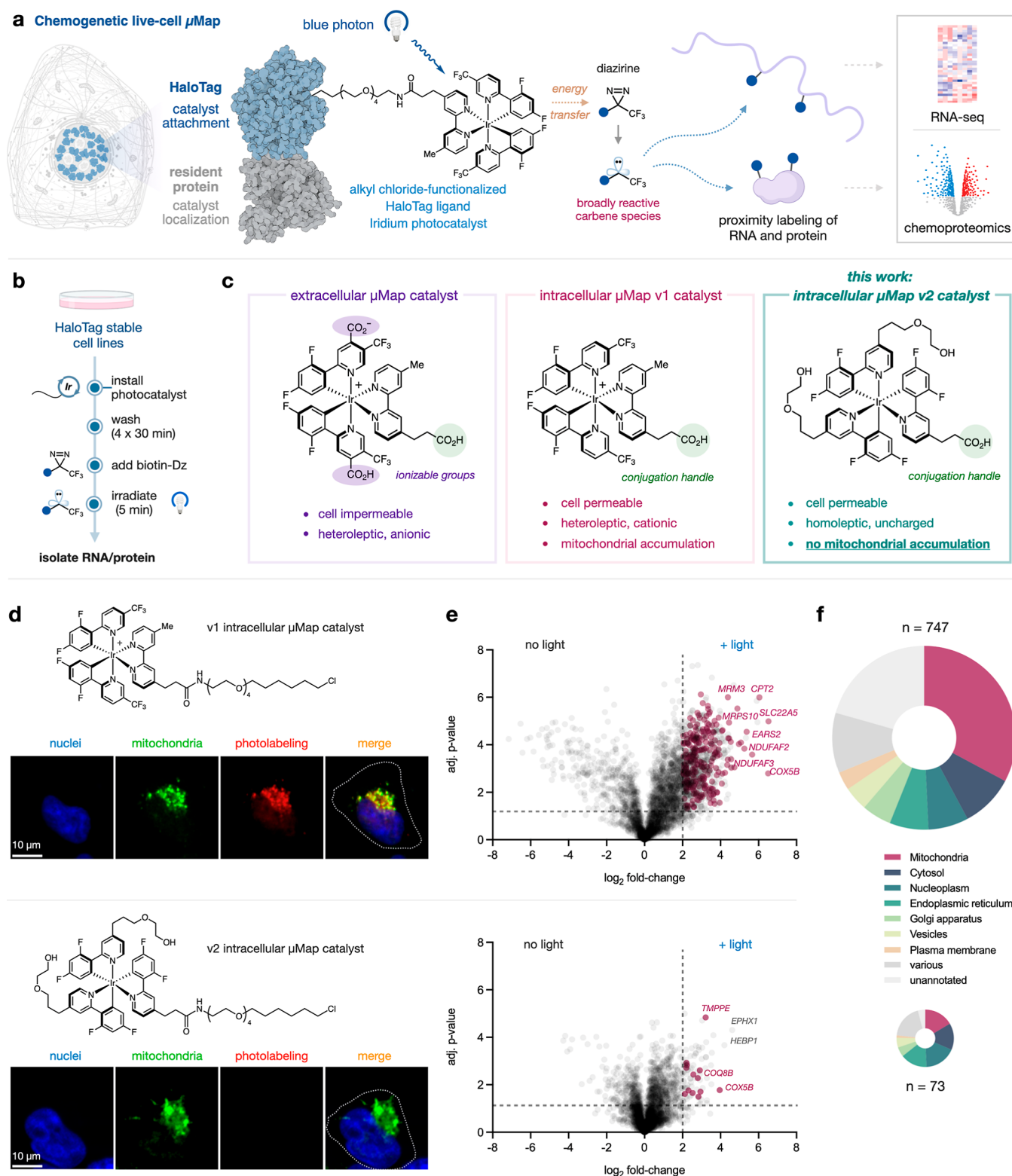
Figure 1. Optimizing a live-cell μMap workflow. (a) μMap using a HaloTag-fused POI and an alkyl chloride-functionalized photocatalyst to label proximal protein and/or RNA molecules. (b) μMap proximity labeling workflow with HaloTag-expressing cells. (c) Structures of μMap catalysts. (d) Immunofluorescence and (e) proteomic evaluation of photolabeling in live cells using version 1 (v1) and v2 μMap Ir catalysts in HEK293T cells. Nuclei stained with Hoechst (blue), mitochondria COXIV (green), and biotinylation stained with streptavidin AF555 (red). Scale bar, 10 μm. Volcano plots depict mitochondrial proteins labeled in red and additional top hits are labeled. (f) Human Protein Atlas subcellular annotation of significant interactors (log_2FC > 2, $p < 0.05$) for both catalysts.

complexes associate with mitochondria,[18] we tested thioxanthone and the homoleptic Ir(dFppy)$_3$ scaffold for labeling activity in vitro. Although both catalysts possess high triplet

energy states (>60 kcal/mol) needed for carbene generation (Figure 1a),[19,20] only Ir(dFppy)$_3$ displayed robust photolabeling (Figure S1). We then synthesized a HaloTag-
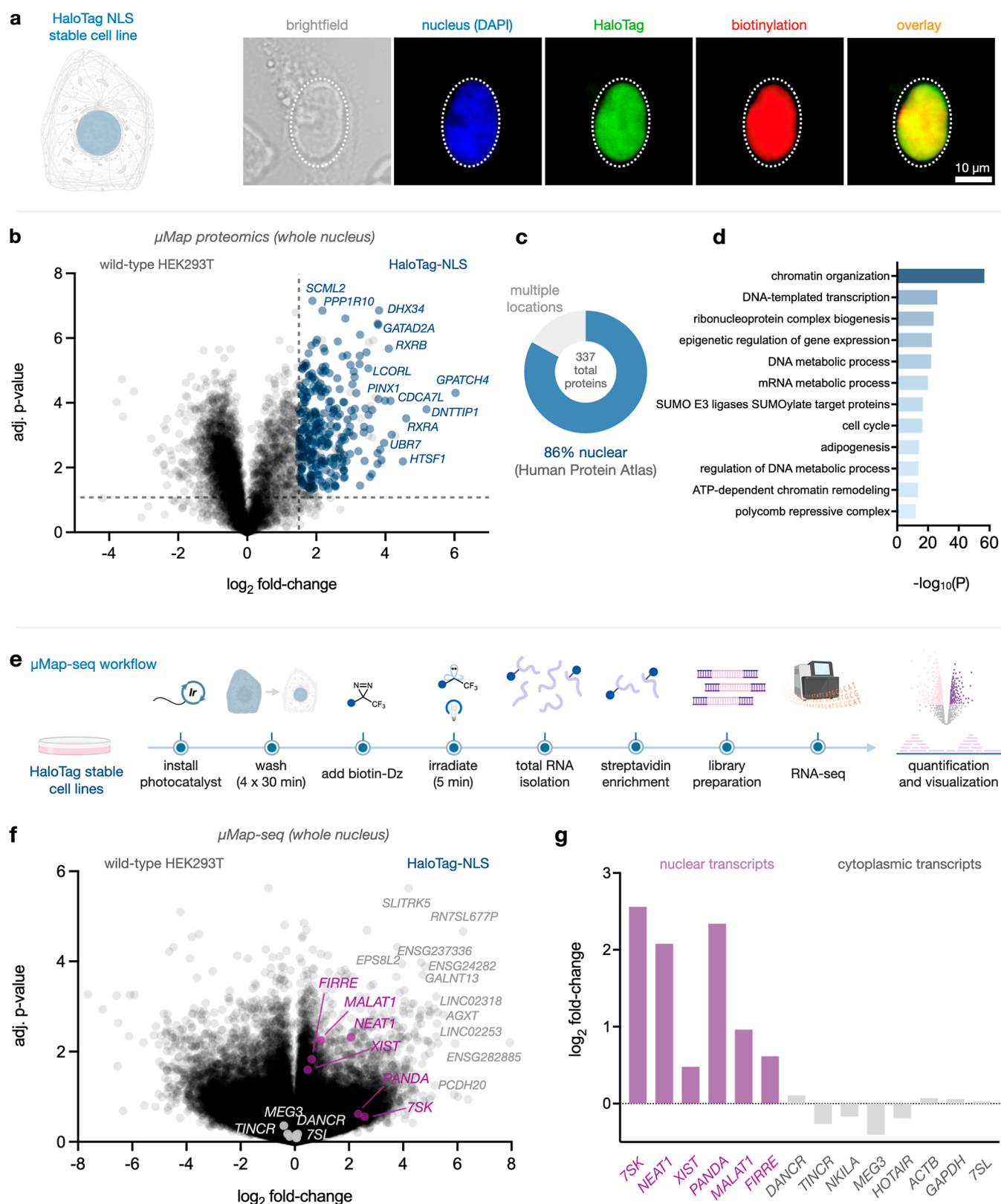
Figure 2. Nuclear proteomic and transcriptomic labeling. (a) Immunofluorescence validation of photolabeling in HaloTag-NLS cells. Nuclei stained with Hoechst (blue), anti-HaloTag (green), and biotinylation stained with streptavidin AF555 (red). Scale bar, 10 μm. (b) Quantitative proteomics in HaloTag-NLS vs wild-type cells with nuclear-annotated proteins (blue). (c) Human Protein Atlas annotation and (d) GO enrichment of interactors. (e) μMap-seq experimental workflow for RNA photolabeling, enrichment, and sequencing. (f,g) μMap-seq of nuclear transcripts with known nuclear transcripts in purple. Several of the top enriched transcripts are also labeled in the volcano plot, with well-known cytosolic transcripts (*MEG3, DANCR, TINCR and 7SL*) at the bottom in gray.

compatible derivative (S10; see Supporting Information for synthetic details) and tested cell permeability in a chloroalkane penetration assay (CAPA).[21] No incorporation was observed compared to the version 1 (v1) catalyst after incubation for 1 h with cells stably expressing HaloTag fused to a nuclear localization signal (NLS) (Figure S2).[22] We hypothesized that hydrophobicity was detrimental, so we appended bis-poly-ethylene glycol groups to increase polarity (Figure 1c). After confirming activity (Figure S3), we reassessed permeability and observed ~30% incorporation (5 μM for 1 h, Figure S4). This short incubation was used to avoid toxicity,[9] so we also measured cell viability under various conditions. The v2 catalyst displayed significantly less toxicity, even at higher concentrations for extended exposures (Figure S5). We identified 10 μM for 16 h as optimal, and high levels (~92%) of HaloTag attachment were observed under these conditions (Figure S6).

We next compared background accumulation of both catalysts by immunofluorescence and quantitative proteomics (Figure 1d,e). HEK293T cells (no HaloTag expression) were separately exposed to each catalyst under their respective conditions followed by media exchanges to wash away unbound catalyst. After incubating with biotin-diazirine, cells were then irradiated with blue light (Figure 1b). Immuno-fluorescence analysis of the v1 catalyst displayed strong mitochondrial labeling overlaying with a COXIV marker, while minimal labeling was detected with the v2 catalyst (Figure 1d). We also quantified off-target interactions by enriching cell lysate for biotinylated proteins followed by label-free liquid chromatography mass spectrometry (LC−MS). Consistent with our immunofluorescence results, the v1 catalyst labeled a significant number of proteins (747 with >2 Log$_2$FC and $p < 0.05$) compared to a nonirradiated control (Figure 1e, Table S1), with the largest distribution identified as mitochondrial via the Human Protein Atlas database (Figure 1f, Table S3).[23] In contrast, the v2 catalyst labeled ~10-fold fewer proteins (73) with a more stochastic distribution (Figure 1e,f, Table S2). These results, combined with efficient HaloTag incorporation and low toxicity, provided confidence in our ability to efficiently profile nuclear structures.

Utilizing cells expressing HaloTag-NLS, we next verified spatial photolabeling control in our workflow by immunostaining with a HaloTag antibody and fluorescent streptavidin to confirm nuclear labeling (Figure 2a). To develop μMap-seq, we assessed RNA labeling in vitro by first incubating total HEK293T RNA with photocatalyst and biotin-diazirine and then irradiating for increasing periods of time. Streptavidin dot blot analysis confirmed photon-limited and catalyst-dependent labeling (Figure S7). We also compared μMap to Halo-seq[24] and chromophore-assisted proximity labeling (CAP-seq),[25] which use bromofluorescein and riboflavin to oxidatively label guanosine (G). Testing catalysts against short (15−20 nt) RNA homopolymers (A, C, U, G) revealed predominant labeling of G-containing strands with Halo-seq and CAP-seq, consistent with their oxidative mechanism (Figure S8a,b). In contrast, μMap was capable of labeling all strands, reflecting the broader reactivity of carbenes. Densitometric quantification of in vitro labeling reactions did display preferential labeling of G- and U-containing strands with μMap (Figure S8c), consistent with recent work suggesting that higher relative nucleophilicity of these bases contributes to greater carbene reactivity.[26] We also evaluated singlet oxygen ($^1O_2$) production from each catalyst via chemiluminescent detection of luminol

oxidation.[27] Irradiation of bromofluorescein and riboflavin expectedly displayed measurable levels of $^1O_2$, while μMap Ir excitation exhibited minimal signal, suggesting a nonoxidative labeling mechanism (Figure S9). In addition, we studied the reaction of a truncated diazirine with individual ribonucleo-sides (A, U, C, G) in DMSO with 1 mol % photocatalyst. LC−MS analysis of reactions enabled identification of several carbene adducts and/or their hydrates (Figure S10). We next tested RNA photolabeling in HaloTag-NLS cells with increasing irradiation; dot blot staining of isolated RNA confirmed transcript biotinylation in cellulo (Figure S11a). Subjecting this material to streptavidin enrichment and quantification also correlated with photolabeling duration (Figure S11b).

Having confirmed RNA reactivity, we then performed parallel proteomic and transcriptomic μMap of the nucleus. Quantitative analysis of HaloTag-NLS labeling identified 337 proteins compared to wild-type cells, including transcription factors, chromatin remodelers, and mediators of DNA metabolism, with 86% of hits nuclear-annotated (Figure 2b−d, Tables S4 and S5).[23] In parallel, we employed a μMap-seq workflow using next-generation sequencing (Figure 2e), and identified thousands of RNAs compared to wild-type cells (Figure 2f). We successfully identified known nuclear-retained long noncoding RNAs (lncRNAs)[28] XIST, NEAT1, MALAT1, 7SK, PANDA, and FIRRE, while known cytosolic transcripts displayed minimal enrichment (Figure 2g, Table S6). Together, these results established feasibility and accuracy of μMap for profiling protein and RNA compositions in subcellular structures.

We next generated stable cell lines expressing different HaloTag-POIs for localization to various organelles (Table 1).

Table 1. μMap Subcellular Locations and Associated HaloTag Fusion Protein Constructs for Catalyst Localization

location	fusion protein construct
nucleus	C-terminal 3X repeat of PKKKRKV nuclear localization sequence (NLS) from simian virus 40[22]
nucleolus	C-terminal 3X repeat of nucleolar targeting sequence MRKKRKKKLRILR from nuclear factor κB-inducing kinase (NIK)[30]
nuclear lamina	C-terminal full-length lamin A (LMNA)[31]
Cajal body	N-terminal full-length COILIN (COIL)[32]
PML body	C-terminal full-length promyelocytic leukemia protein isoform IV (PML)[33]
paraspeckle	C-terminal full-length Non-POU domain containing octamer binding (NONO)[34]

We first profiled the nucleolus, and immunofluorescence validation of μMap again exhibited high spatial labeling control (Figure 3a). Quantitative proteomics identified 74 enriched interactors (log$_2$FC > 1.5, $p < 0.05$), of which 49 (66%) are previously validated nucleolar proteins (Figure 3b,c, Table S8). Additionally, μMap enriched both ribosomal subunits as well as assembly machinery, and gene ontology (GO) analysis correctly ascribed these known functions (Figure 3b−d, Table S9).[29] We also identified 25 proteins that were either associated with multiple subcellular locations or were not previously observed to localize in the nucleolus. We selected three enriched proteins from our nucleolar μMap data set for further validation, including heme binding protein 1 (HEBP1), KN motif and ankyrin repeat domains 1 (KANK1), and
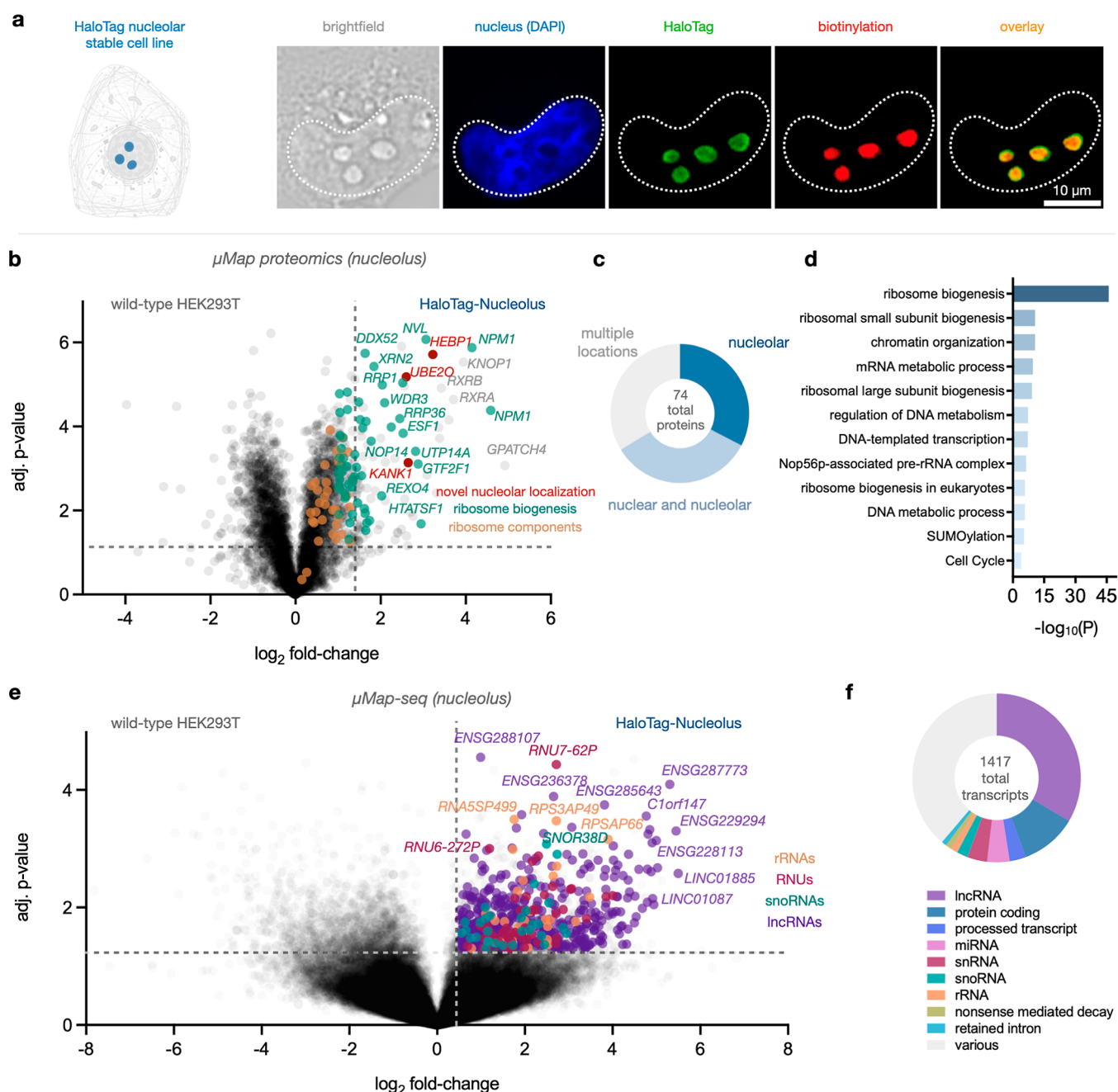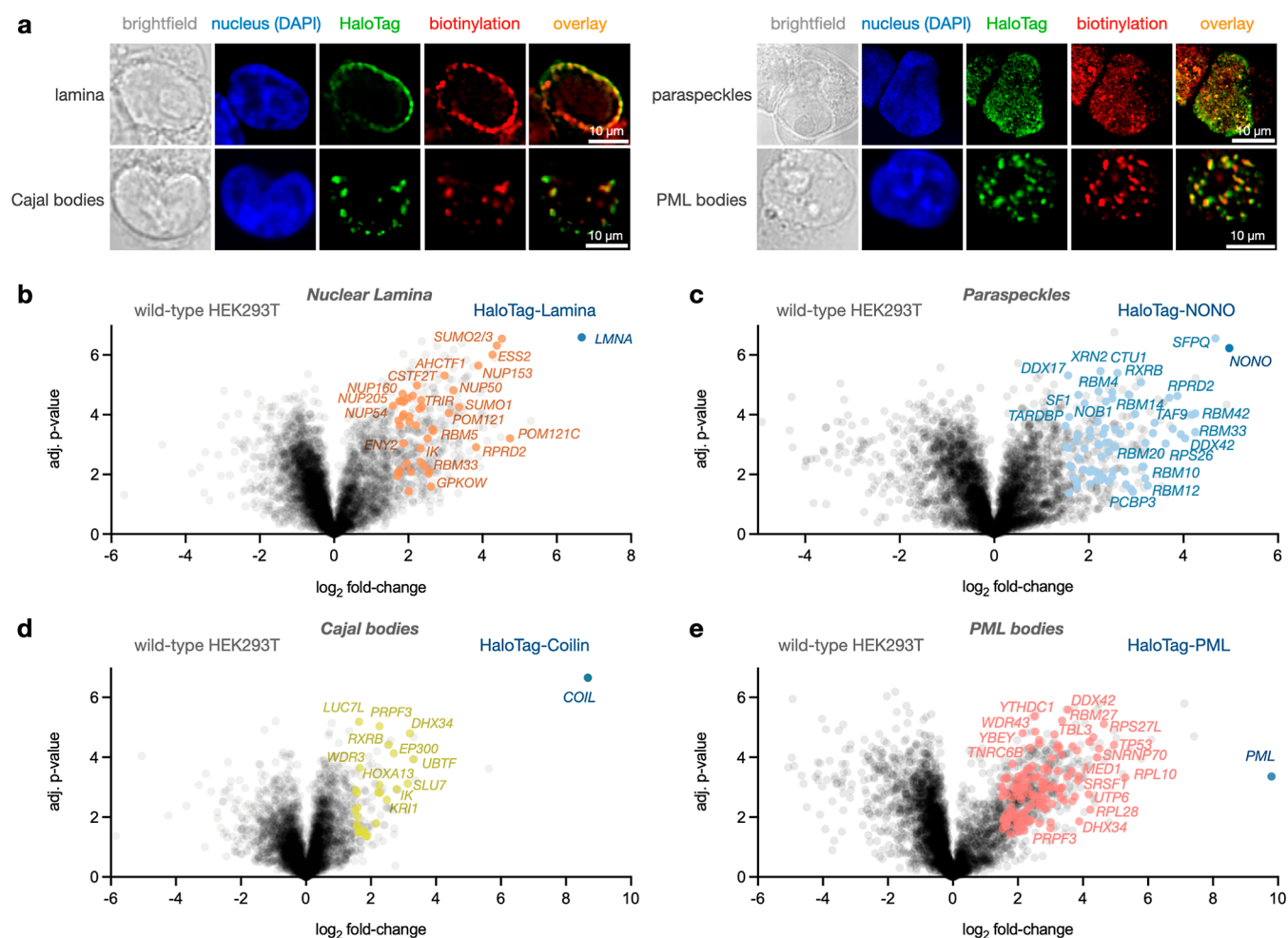
Figure 3. Nucleolar μMap. (a) Immunofluorescence validation of nucleolar photolabeling. Nuclei stained with Hoechst (blue), anti-HaloTag (green), and biotinylation stained with streptavidin AF555 (red). Scale bar, 10 μm. (b) Quantitative proteomics in HaloTag-NIK vs wild-type cells. Ribosomal protein subunits (orange) and ribosomal biogenesis machinery (green), novel nucleolar interactors (red). (c) Human Protein Atlas annotation and (d) GO enrichment analysis of nucleolar interactors. (e,f) μMap-seq of nucleolar transcripts. Several top hits are annotated and data points colored by transcript type.

ubiquitin conjugating enzyme E2 O (UBE2O) (Figure 3b, red data points). Immunofluorescence microscopy confirmed at least partial subcellular localization to the nucleolus in all 3 candidates (Figure S12). Although the biochemical or cellular consequences of this localization are not fully known, these results support the accuracy of μMap platform and highlight the utility of proximity labeling for discovering new protein localization signatures.

Nucleolar μMap-seq was performed in parallel, and expectedly identified many small nuclear (snRNA) and nucleolar RNAs (snoRNAs) (Figure 3e, Table S10). Despite rRNA depletion in our library preparation workflow, we also

identified rRNA pseudogenes, likely reflecting minor sequence differences that evade depletion probes but also confirm the known presence of ribosomes in the nucleolus. We were also surprised that the majority of identified transcripts were long noncoding RNAs (lncRNAs) (Figure 3f), with many containing no functional annotations (ENSG00000287773, ENSG00000229294, LINC01885, among others, Figure 3e). Recent reports have identified nucleolar lncRNAs that regulate rRNA transcription, stress response, and nucleolar structure,[35−38] underscoring the potential impact of these novel associations. Together, our results validate μMap for proteomic and transcriptomic profiling of subnuclear structures, in turn

Figure 4. μMap profiling across nuclear locations. (a) Immunofluorescence validation of photolabeling with each stable cell line. Nuclei stained with Hoechst (blue), anti-HaloTag (green), and biotinylation stained with streptavidin AF555 (red). Scale bars, 10 μm. (b−e) Quantitative μMap proteomics in each HaloTag cell line vs wild-type cells. Highlighted proteins denote hits with RNA or DNA-related functions.

identifying known roles for the nucleolus and highlighting new potential functions.

Expanding on these results, we next performed μMap profiling across the lamina, Cajal bodies, paraspeckles, and PML bodies. Immunofluorescence analysis confirmed restriction of labeling to nuclear membranes or condensates, again reflecting high spatiotemporal labeling control (Figure 4a).

Quantitative μMap proteomics displayed robust enrichment of each HaloTag-POI (*LMNA, NONO, COIL, PML*), and for each location we annotated interactors relating to its purported RNA or DNA-related functions ($log_2FC > 1.5$, $p < 0.05$, Figure 4b−e, Tables S11−S18). Proximal proteins identified in the lamina included nucleoporins and other pore complex members (*POM121, NUP153, NUP50, NUP54, NUP160, NUP205*) (Figure 4b, Table S11),[39] and 44 proteins with known roles in DNA and RNA-related functions (Figure 4b, orange data points). HaloTag-NONO μMap enriched the core paraspeckle proteins *NONO, FUS, PSPC1, EWSR1, CPSF7* and *SFPQ*,[34] as well as 13 RNA-binding motif (*RBM*) proteins, with 76 proteins identified with previous associations in RNA processing (Figure 4c, light blue).[40] Cajal body profiling identified 28 proteins involved in RNA metabolism (Figure 4d, yellow data points, including *DHX34, SLU7,* and *PRPF3*), and μMap of PML bodies enriched greater than 100 interactors relating to transcript processing (*DDX42*,[41] *RBM27*[42]) and

gene regulation (*MED1*,[43] *TBL3*[44]) (Figure 4e, pink data points). We then compared all proteomic data sets via comparative GO enrichment to ascribe potential functional roles for each structure (Figure 5, Tables S8−18). The nucleolus was expectedly enriched in ribosomal biosynthetic functions,[29] while other organelles were associated with rRNA transcriptional repression. The lamina was linked with nuclear envelope regulation, nucleocytoplasmic transport, DNA replication, repair, and transcription.[39] Our results also suggested paraspeckles may participate in RNA splicing while also associating with chromatin silencing through *SWI/SNF*, in agreement with emerging functional explorations.[40,45] Current hypotheses implicate PML bodies in gene expression regulation, DNA repair, and infection stress responses,[33,46] and we observed overlap with laminar functions that may suggest new physical roles and associations with the nuclear envelope. In particular, the PML interactome was linked with DNA repair and transcript export, the latter of which is not a currently known role. We also confirmed associations with both chromatin modification and telomere maintenance, in line with recent experimental evidence.[47,48] PML bodies were also associated with RNA metabolism, and our results suggest a possible role in 3′ end processing and polyadenylation. Cajal bodies are hypothesized to facilitate small nuclear ribonucleoprotein biogenesis as well as long transcript processing.[32,49,50]

Figure 5. Comparative gene ontology (GO) enrichment from μMap proteomic profiling across the nucleolus, nuclear lamina, cajal bodies, paraspeckles, and PML bodies. Red heatmap scores highlight enriched biological processes and molecular functions, with intensity correlating to enrichment significance ($-\log_{10} P$).

We observed ontological enrichment of spliceosomal activity as well as potential roles in mRNA 5′ capping and regulating chromatin organization and transcription.

In parallel, we performed μMap-seq across all 5 subnuclear locations to catalog proximal RNA species. To gain insight into both the types of transcripts and different isoforms that were enriched, transcript-level quantification of RNA hits was performed (>3 $\log_2$FC and $p < 0.05$, Tables S19−S23), which revealed distinct populations across all organelles (Figure 6a) with differential transcript type enrichment (Figure 6b). Protein-coding mRNAs were predominantly identified in each location, but different structures also enriched certain RNA types compared to other organelles. We again observed that the nucleolus contained the highest proportion of lncRNAs, and while recent studies point to possible structural roles for these transcripts,[35−38] the full biological significance remains unclear and warrants further study. Paraspeckle μMap-seq also identified a large proportion of lncRNAs, consistent with known associations with these transcripts.[51] Combined with proteomic data, these results suggest paraspeckles may participate in lncRNA splicing and processing. Conversely, the lamina identified the lowest lncRNA percentage, yet was highly enriched in nonsense-mediated mRNA decay transcripts, potentially indicating nucleocytoplasmic accumulation for subsequent surveillance and degradation.[52] PML body functions are not currently well understood, though our combined results suggest possible roles in transcriptional activation[53] and retained intron processing, in line with recent studies suggesting this regulates cell cycle progression.[54] Although our data suggest these potential roles for paraspeckles in RNA splicing and chromatin silencing, as well as possible novel functions for PML bodies in transcript processing and export, the localization of a protein or RNA transcript does not inherently indicate its function, and further work is needed to validate the biological significance and underlying mechanisms of these processes. Additionally, the use of Halotag fusion constructs, while a validated and useful tool in chemical biology, can require careful confirmation studies due to the potential for perturbing natural cellular behavior. Together, these results highlight the utility of spatial proteomics and transcriptomics, supporting previous functional notions of different structures and pointing to new possible roles for nuclear condensates.
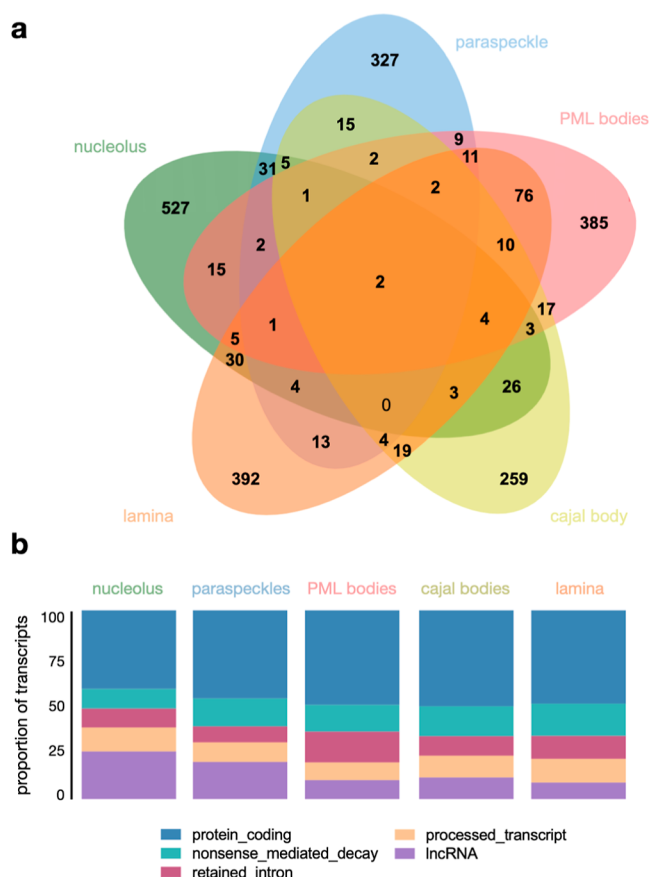
Figure 6. μMap-seq transcriptional profiling across subnuclear locations. (a) Transcript-level comparison of enriched RNAs between locations. (b) Stacked bar graph displaying enriched transcript types.

In conclusion, we disclose here a new chemogenetic platform for performing μMap analysis in living cells that is well-tolerated and exhibits minimal background. We use our new workflow to generate a proteomic and transcriptomic map across 5 subnuclear locations, providing new potential insights toward deciphering cellular roles of specific structures. Intracellular μMap is a generalizable tool, and we envision that this technology can be deployed across a variety of biological settings, in turn elucidating cellular mechanisms, identifying disease pathologies, and accelerating the discovery of new therapeutic targets.

■ ASSOCIATED CONTENT

ⓢ Supporting Information

The Supporting Information is available free of charge at https://pubs.acs.org/doi/10.1021/jacs.4c11612.

Experimental procedures and supplementary figures (PDF)

Proteomic and RNA-seq data sets and analyses (XLSX)

Proteomic and RNA-seq data sets and analyses (XLSX)

■ AUTHOR INFORMATION

Corresponding Author

David W. C. MacMillan − Department of Chemistry, Princeton University, Princeton, New Jersey 08544, United States; Merck Center for Catalysis at Princeton University, Princeton, New Jersey 08544, United States; orcid.org/0000-0001-6447-0587; Email: dmacmill@princeton.edu

Authors

Steve D. Knutson − Department of Chemistry, Princeton University, Princeton, New Jersey 08544, United States; Merck Center for Catalysis at Princeton University, Princeton, New Jersey 08544, United States

Chenmengxiao Roderick Pan − Department of Chemistry, Princeton University, Princeton, New Jersey 08544, United States; Merck Center for Catalysis at Princeton University, Princeton, New Jersey 08544, United States

Niels Bisballe − Department of Chemistry, Princeton University, Princeton, New Jersey 08544, United States; Merck Center for Catalysis at Princeton University, Princeton, New Jersey 08544, United States; orcid.org/0000-0002-4476-5481

Brandon J. Bloomer − Department of Chemistry, Princeton University, Princeton, New Jersey 08544, United States; Merck Center for Catalysis at Princeton University, Princeton, New Jersey 08544, United States

Philip Raftopolous − Department of Chemistry, Princeton University, Princeton, New Jersey 08544, United States; Merck Center for Catalysis at Princeton University, Princeton, New Jersey 08544, United States

Iakovos Saridakis − Department of Chemistry, Princeton University, Princeton, New Jersey 08544, United States; Merck Center for Catalysis at Princeton University, Princeton, New Jersey 08544, United States; orcid.org/0000-0002-2690-5401

Complete contact information is available at:
https://pubs.acs.org/10.1021/jacs.4c11612

Author Contributions

The manuscript was written through contributions of all authors. All authors have given approval on the final version of the manuscript.

Notes

The authors declare the following competing financial interest(s): DWCM declares an ownership interest in the company Dexterity Pharma LLC, which has commercialized materi-als used in this work.

■ ACKNOWLEDGMENTS

■ REFERENCES

(1) Sabari, B. R.; Dall'Agnese, A.; Young, R. A. Biomolecular condensates in the nucleus. *Trends Biochem. Sci.* **2020**, 45 (11), 961−977.

(2) Boeynaems, S.; Chong, S.; Gsponer, J.; Holt, L.; Milovanovic, D.; Mitrea, D. M.; Mueller-Cajar, O.; Portz, B.; Reilly, J. F.;

Reinkemeier, C. D.; et al. Phase separation in biology and disease; current perspectives and open questions. *J. Mol. Biol.* **2023**, *435* (5), 167971.

(3) Mathieu, C.; Pappu, R. V.; Taylor, J. P. Beyond aggregation: Pathological phase transitions in neurodegenerative disease. *Science* **2020**, *370* (6512), 56−60.

(4) Spannl, S.; Tereshchenko, M.; Mastromarco, G. J.; Ihn, S. J.; Lee, H. O. Biomolecular condensates in neurodegeneration and cancer. *Traffic* **2019**, *20* (12), 890−911.

(5) Geri, J. B.; Oakley, J. V.; Reyes-Robles, T.; Wang, T.; McCarver, S. J.; White, C. H.; Rodriguez-Rivera, F. P.; Parker, D. L., Jr.; Hett, E. C.; Fadeyi, O. O.; et al. Microenvironment mapping via Dexter energy transfer on immune cells. *Science* **2020**, *367* (6482), 1091−1097.

(6) Oakley, J. V.; Buksh, B. F.; Fernández, D. F.; Oblinsky, D. G.; Seath, C. P.; Geri, J. B.; Scholes, G. D.; MacMillan, D. W. Radius measurement via super-resolution microscopy enables the development of a variable radii proximity labeling platform. *Proc. Natl. Acad. Sci. U.S.A.* **2022**, *119* (32), No. e2203027119.

(7) Meyer, C. F.; Seath, C. P.; Knutson, S. D.; Lu, W.; Rabinowitz, J. D.; MacMillan, D. W. Photoproximity labeling of sialylated glycoproteins (GlycoMap) reveals sialylation-dependent regulation of ion transport. *J. Am. Chem. Soc.* **2022**, *144* (51), 23633−23641.

(8) Huth, S. W.; Oakley, J. V.; Seath, C. P.; Geri, J. B.; Trowbridge, A. D.; Parker, D. L., Jr.; Rodriguez-Rivera, F. P.; Schwaid, A. G.; Ramil, C.; Ryu, K. A.; et al. μMap Photoproximity Labeling Enables Small Molecule Binding Site Mapping. *J. Am. Chem. Soc.* **2023**, *145* (30), 16289−16296.

(9) Trowbridge, A. D.; Seath, C. P.; Rodriguez-Rivera, F. P.; Li, B. X.; Dul, B. E.; Schwaid, A. G.; Buksh, B. F.; Geri, J. B.; Oakley, J. V.; Fadeyi, O. O.; et al. Small molecule photocatalysis enables drug target identification via energy transfer. *Proc. Natl. Acad. Sci. U.S.A.* **2022**, *119* (34), No. e2208077119.

(10) Seath, C. P.; Burton, A. J.; Sun, X.; Lee, G.; Kleiner, R. E.; MacMillan, D. W.; Muir, T. W. Tracking chromatin state changes using nanoscale photo-proximity labelling. *Nature* **2023**, *616* (7957), 574−580.

(11) Pan, C. R.; Knutson, S. D.; Huth, S. W.; MacMillan, D. W. μMap proximity labeling in living cells reveals stress granule disassembly mechanisms. *Nat. Chem. Biol.* **2024**, 1−11.

(12) Huang, Z.; Liu, Z.; Xie, X.; Zeng, R.; Chen, Z.; Kong, L.; Fan, X.; Chen, P. R. Bioorthogonal photocatalytic decaging-enabled mitochondrial proteomics. *J. Am. Chem. Soc.* **2021**, *143* (44), 18714−18720.

(13) Liu, Z.; Guo, F.; Zhu, Y.; Qin, S.; Hou, Y.; Guo, H.; Lin, F.; Chen, P. R.; Fan, X. Bioorthogonal photocatalytic proximity labeling in primary living samples. *Nat. Commun.* **2024**, *15* (1), 2712.

(14) Wang, H.; Zhang, Y.; Zeng, K.; Qiang, J.; Cao, Y.; Li, Y.; Fang, Y.; Zhang, Y.; Chen, Y. Selective mitochondrial protein labeling enabled by biocompatible photocatalytic reactions inside live cells. *JACS Au* **2021**, *1* (7), 1066−1075.

(15) Kuang, S.; Wei, F.; Karges, J.; Ke, L.; Xiong, K.; Liao, X.; Gasser, G.; Ji, L.; Chao, H. Photodecaging of a mitochondria-localized iridium (III) endoperoxide complex for two-photon photoactivated therapy under hypoxia. *J. Am. Chem. Soc.* **2022**, *144* (9), 4091−4101.

(16) Huang, H.; Banerjee, S.; Qiu, K.; Zhang, P.; Blacque, O.; Malcomson, T.; Paterson, M. J.; Clarkson, G. J.; Staniforth, M.; Stavros, V. G.; et al. Targeted photoredox catalysis in cancer cells. *Nat. Chem.* **2019**, *11* (11), 1041−1048.

(17) Los, G. V.; Encell, L. P.; McDougall, M. G.; Hartzell, D. D.; Karassina, N.; Zimprich, C.; Wood, M. G.; Learish, R.; Ohana, R. F.; Urh, M.; et al. HaloTag: a novel protein labeling technology for cell imaging and protein analysis. *ACS Chem. Biol.* **2008**, *3* (6), 373−382.

(18) Hoye, A. T.; Davoren, J. E.; Wipf, P.; Fink, M. P.; Kagan, V. E. Targeting mitochondria. *Acc. Chem. Res.* **2008**, *41* (1), 87−97.

(19) Nikitas, N. F.; Gkizis, P. L.; Kokotos, C. G. Thioxanthone: a powerful photocatalyst for organic reactions. *Org. Biomol. Chem.* **2021**, *19* (24), 5237−5253.

(20) Teegardin, K.; Day, J. I.; Chan, J.; Weaver, J. Advances in photocatalysis: a microreview of visible light mediated ruthenium and iridium catalyzed organic transformations. *Org. Process Res. Dev.* **2016**, *20* (7), 1156−1163.

(21) Peraro, L.; Deprey, K. L.; Moser, M. K.; Zou, Z.; Ball, H. L.; Levine, B.; Kritzer, J. A. Cell penetration profiling using the chloroalkane penetration assay. *J. Am. Chem. Soc.* **2018**, *140* (36), 11360−11369.

(22) Lu, J.; Wu, T.; Zhang, B.; Liu, S.; Song, W.; Qiao, J.; Ruan, H. Types of nuclear localization signals and mechanisms of protein import into the nucleus. *Cell Commun. Signaling* **2021**, *19* (1), 60.

(23) Thul, P. J.; Åkesson, L.; Wiking, M.; Mahdessian, D.; Geladaki, A.; Ait Blal, H.; Alm, T.; Asplund, A.; Björk, L.; Breckels, L. M.; et al. A subcellular map of the human proteome. *Science* **2017**, *356* (6340), No. eaal3321.

(24) Engel, K. L.; Lo, H.-Y. G.; Goering, R.; Li, Y.; Spitale, R. C.; Taliaferro, J. M. Analysis of subcellular transcriptomes by RNA proximity labeling with Halo-seq. *Nucleic Acids Res.* **2022**, *50* (4), No. e24.

(25) Wang, P.; Tang, W.; Li, Z.; Zou, Z.; Zhou, Y.; Li, R.; Xiong, T.; Wang, J.; Zou, P. Mapping spatial transcriptome with light-activated proximity-dependent RNA labeling. *Nat. Chem. Biol.* **2019**, *15* (11), 1110−1119.

(26) Lee, Y.-H.; Yu, E.; Park, C.-M. Programmable site-selective labeling of oligonucleotides based on carbene catalysis. *Nat. Commun.* **2021**, *12* (1), 1681.

(27) Wang, D. M.; Zhang, Y.; Zheng, L. L.; Yang, X. X.; Wang, Y.; Huang, C. Z. Singlet oxygen involved luminol chemiluminescence catalyzed by graphene oxide. *J. Phys. Chem. C* **2012**, *116* (40), 21622−21628.

(28) Statello, L.; Guo, C.-J.; Chen, L.-L.; Huarte, M. Gene regulation by long non-coding RNAs and its biological functions. *Nat. Rev. Mol. Cell Biol.* **2021**, *22* (2), 96−118.

(29) Mélèse, T.; Xue, Z. The nucleolus: an organelle formed by the act of building a ribosome. *Curr. Opin. Cell Biol.* **1995**, *7* (3), 319−324.

(30) Birbach, A.; Bailey, S. T.; Ghosh, S.; Schmid, J. A. Cytosolic, nuclear and nucleolar localization signals determine subcellular distribution and activity of the NF-κB inducing kinase NIK. *J. Cell Sci.* **2004**, *117* (16), 3615−3624.

(31) Worman, H. J. Nuclear lamins and laminopathies. *J. Pathol.* **2012**, *226* (2), 316−325.

(32) Machyna, M.; Kehr, S.; Straube, K.; Kappei, D.; Buchholz, F.; Butter, F.; Ule, J.; Hertel, J.; Stadler, P. F.; Neugebauer, K. M. The coilin interactome identifies hundreds of small noncoding RNAs that traffic through Cajal bodies. *Mol. Cell* **2014**, *56* (3), 389−399.

(33) Shen, T. H.; Lin, H.-K.; Scaglioni, P. P.; Yung, T. M.; Pandolfi, P. P. The mechanisms of PML-nuclear body formation. *Mol. Cell* **2006**, *24* (3), 331−339.

(34) Passon, D. M.; Lee, M.; Rackham, O.; Stanley, W. A.; Sadowska, A.; Filipovska, A.; Fox, A. H.; Bond, C. S. Structure of the heterodimer of human NONO and paraspeckle protein component 1 and analysis of its role in subnuclear body formation. *Proc. Natl. Acad. Sci. U.S.A.* **2012**, *109* (13), 4846−4850.

(35) Wu, M.; Xu, G.; Han, C.; Luan, P.-F.; Xing, Y.-H.; Nan, F.; Yang, L.-Z.; Huang, Y.; Yang, Z.-H.; Shan, L.; et al. lncRNA SLERT controls phase separation of FC/DFCs to facilitate Pol I transcription. *Science* **2021**, *373* (6554), 547−555.

(36) Feng, S.; Desotell, A.; Ross, A.; Jovanovic, M.; Manley, J. L. A nucleolar long "non-coding" RNA encodes a novel protein that functions in response to stress. *Proc. Natl. Acad. Sci. U.S.A.* **2023**, *120* (9), No. e2221109120.

(37) Pirogov, S. A.; Gvozdev, V. A.; Klenov, M. S. Long noncoding RNAs and stress response in the nucleolus. *Cells* **2019**, *8* (7), 668.

(38) Caudron-Herger, M.; Pankert, T.; Rippe, K. Regulation of nucleolus assembly by non-coding RNA polymerase II transcripts. *Nucleus* **2016**, *7* (3), 308−318.

(39) Wong, X.; Melendez-Perez, A. J.; Reddy, K. L. The nuclear lamina. *Cold Spring Harbor Perspect. Biol.* **2022**, *14* (2), a040113.

(40) Wang, Y.; Chen, L.-L. Organization and function of paraspeckles. *Essays Biochem.* **2020**, *64* (6), 875−882.

(41) Yang, F.; Bian, T.; Zhan, X.; Chen, Z.; Xing, Z.; Larsen, N. A.; Zhang, X.; Shi, Y. Mechanisms of the RNA helicases DDX42 and DDX46 in human U2 snRNP assembly. *Nat. Commun.* **2023**, *14* (1), 897.

(42) Silla, T.; Schmid, M.; Dou, Y.; Garland, W.; Milek, M.; Imami, K.; Johnsen, D.; Polak, P.; Andersen, J. S.; Selbach, M.; et al. The human ZC3H3 and RBM26/27 proteins are critical for PAXT-mediated nuclear RNA decay. *Nucleic Acids Res.* **2020**, *48* (5), 2518–2530.

(43) Bellacosa, A. Role of MED1 (MBD4) Gene in DNA repair and human cancer. *J. Cell. Physiol.* **2001**, *187* (2), 137–144.

(44) Choi, H. K.; Choi, K. C.; Kang, H. B.; Lee, Y. H.; Yoo, J. Y.; Song, I. J.; Yoon, H. G. Function of multiple LisH/WD-40 repeat-containing proteins in feed-forward transcriptional repression by SMRT/N-CoR corepressor complexes. *FASEB J.* **2008**, *22* (S2), 200.

(45) Reddy, D.; Bhattacharya, S.; Levy, M.; Zhang, Y.; Gogol, M.; Li, H.; Florens, L.; Workman, J. L. Paraspeckles interact with SWI/SNF subunit ARID1B to regulate transcription and splicing. *EMBO Rep.* **2023**, *24* (1), No. e55345.

(46) Lallemand-Breitenbach, V.; de Thé, H. PML nuclear bodies: from architecture to function. *Curr. Opin. Cell Biol.* **2018**, *52*, 154–161.

(47) Corpet, A.; Kleijwegt, C.; Roubille, S.; Juillard, F.; Jacquet, K.; Texier, P.; Lomonte, P. PML nuclear bodies and chromatin dynamics: catch me if you can. *Nucleic Acids Res.* **2020**, *48* (21), 11890–11912.

(48) Chang, F. T.; McGhie, J. D.; Chan, F. L.; Tang, M. C.; Anderson, M. A.; Mann, J. R.; Andy Choo, K.; Wong, L. H. PML bodies provide an important platform for the maintenance of telomeric chromatin integrity in embryonic stem cells. *Nucleic Acids Res.* **2013**, *41* (8), 4447–4458.

(49) Gall, J. G. The centennial of the Cajal body. *Nat. Rev. Mol. Cell Biol.* **2003**, *4* (12), 975–980.

(50) Wang, Q.; Sawyer, I. A.; Sung, M.-H.; Sturgill, D.; Shevtsov, S. P.; Pegoraro, G.; Hakim, O.; Baek, S.; Hager, G. L.; Dundr, M. Cajal bodies are linked to genome conformation. *Nat. Commun.* **2016**, *7* (1), 10966.

(51) Fox, A. H.; Nakagawa, S.; Hirose, T.; Bond, C. S. Paraspeckles: where long noncoding RNA meets phase separation. *Trends Biochem. Sci.* **2018**, *43* (2), 124–135.

(52) Hug, N.; Longman, D.; Cáceres, J. F. Mechanism and regulation of the nonsense-mediated decay pathway. *Nucleic Acids Res.* **2016**, *44* (4), 1483–1495.

(53) LaMorte, V. J.; Dyck, J. A.; Ochs, R. L.; Evans, R. M. Localization of nascent RNA and CREB binding protein with the PML-containing nuclear body. *Proc. Natl. Acad. Sci. U.S.A.* **1998**, *95* (9), 4991–4996.

(54) Barutcu, A. R.; Wu, M.; Braunschweig, U.; Dyakov, B. J.; Luo, Z.; Turner, K. M.; Durbic, T.; Lin, Z.-Y.; Weatheritt, R. J.; Maass, P. G.; et al. Systematic mapping of nuclear domain-associated transcripts reveals speckles and lamina as hubs of functionally distinct retained introns. *Mol. Cell* **2022**, *82* (5), 1035–1052.e9.